nature materials

ARTICLES

PUBLISHED ONLINE: 29 AUGUST 2016 | DOI: 10.1038/NMAT4726

Highly efficient and tunable spin-to-charge conversion through Rashba coupling at oxide interfaces

E. Lesne[1†‡], Yu Fu[2†], S. Oyarzun[2,3], J. C. Rojas-Sánchez[1*‡], D. C. Vaz[1], H. Naganuma[1,4], G. Sicoli[5], J.-P. Attané[2], M. Jamet[2], E. Jacquet[1], J.-M. George[1], A. Barthélémy[1], H. Jaffrès[1], A. Fert[1], M. Bibes[1*] and L. Vila[2]

The spin–orbit interaction couples the electrons' motion to their spin. As a result, a charge current running through a material with strong spin–orbit coupling generates a transverse spin current (spin Hall effect, SHE) and vice versa (inverse spin Hall effect, ISHE). The emergence of SHE and ISHE as charge-to-spin interconversion mechanisms offers a variety of novel spintronic functionalities and devices, some of which do not require any ferromagnetic material. However, the interconversion efficiency of SHE and ISHE (spin Hall angle) is a bulk property that rarely exceeds ten percent, and does not take advantage of interfacial and low-dimensional effects otherwise ubiquitous in spintronic hetero- and mesostructures. Here, we make use of an interface-driven spin–orbit coupling mechanism—the Rashba effect—in the oxide two-dimensional electron system (2DES) $LaAlO_3/SrTiO_3$ to achieve spin-to-charge conversion with unprecedented efficiency. Through spin pumping, we inject a spin current from a NiFe film into the oxide 2DES and detect the resulting charge current, which can be strongly modulated by a gate voltage. We discuss the amplitude of the effect and its gate dependence on the basis of the electronic structure of the 2DES and highlight the importance of a long scattering time to achieve efficient spin-to-charge interconversion.

Perovskite oxide materials possess a broad range of functionalities[1], some of which can be very appealing for spintronics[2]. This includes half-metallicity in mixed-valence manganites—which can be used to produce giant tunnel magnetoresistance[3]—or multiferroicity—through which the magnetization direction can be electrically controlled at low power[4]. Recent years have seen the emergence of novel spintronics effects[5–7] based on the generation and control of pure spin currents through spin–orbit effects in semiconducting and metallic systems[8–10]. However, despite a renewal of interest for 4*d* and 5*d* transition metal perovksites[11], spin–orbit effects remained largely unexplored in oxide spintronics.

An emerging direction in oxide research aims at discovering novel electronic phases at interfaces between two oxide materials[12]. A well-known example is the $LaAlO_3/SrTiO_3$ system: while both $LaAlO_3$ (LAO) and $SrTiO_3$ (STO) are wide bandgap insulators, a high-mobility two-dimensional electron system (2DES) forms at their interface[13] if the LAO thickness is at least 4 unit cells (uc)[14]. Interestingly, LAO/STO possesses several remarkable extra functionalities, including a gate-tunable Rashba effect[15,16], which makes it particularly appealing for spintronics[17–19].

The Rashba effect is a manifestation of the spin–orbit interaction (SOI) in solids, where spin degeneracy associated with the spatial inversion symmetry is lifted due to a symmetry-breaking electric field normal to a heterointerface[20,21]. In a Rashba 2DES, the flow of a charge current results in the creation of a non-zero spin accumulation[22,23] coming from uncompensated spin-textured Fermi surfaces. Recently, the converse effect, the so-called inverse Edelstein effect (IEE)—that is a spin-to-charge conversion through SOI—was discovered at Ag/Bi(111) interfaces[24]. Here, we report the observation of a very large, gate-tunable IEE in NiFe/LAO//STO heterostructures, with a spin-to-charge conversion efficiency more than one order of magnitude larger than at the Ag/Bi(111) interface or in spin Hall materials.

NiFe/LAO//STO samples were grown in a set-up combining pulsed laser deposition (PLD) and sputtering chambers with *in vacuo* sample transfer (see Methods). Following our previous report on Co-capped LAO//STO samples[25], we exploit the possibility to reduce the critical LAO thickness required for 2DES formation below 4 uc through metal capping. Starting with TiO_2-terminated STO single-crystal substrates, we first grow a 2-uc-thick LAO film by PLD. As visible on the reflection high-energy electron diffraction (RHEED) images and intensity oscillations (Fig. 1a), the growth proceeds layer by layer. We then deposit a permalloy ($Ni_{81}Fe_{19}$) film (2.5 or 20 nm thick) by d.c. sputtering and cap it with aluminium (for transport experiments) or gold (for transmission electron microscopy, TEM). As evidenced by atomic force microscopy, the sample surface is smooth, retaining the step-and-terrace topography of the STO substrate and LAO film (see Fig. 1b). TEM images (Fig. 1c) confirm the good crystallinity of the 2-uc LAO layer and indicate a nanocrystalline structure for the 2 nm NiFe film and the Au cap

---

[1]Unité Mixte de Physique, CNRS, Thales, Univ. Paris-Sud, Université Paris-Saclay, 91767 Palaiseau, France. [2]Spintec, Institut Nanosciences et Cryogenie, Univ. Grenoble Alpes, CEA, CNRS, F-38000 Grenoble, France. [3]Departamento de Física, CEDENNA, Universidad de Santiago de Chile (USACH), Avenida Ecuador 3493, 9170124 Santiago, Chile. [4]Tohoku University, Department of Applied Physics, 6-6-05 Aoba, Aramaki, Aoba, Sendai 980-8579, Japan. [5]Institut Nanosciences et Cryogenie, Univ. Grenoble Alpes, CEA, F-38000 Grenoble, France. †These authors contributed equally to this work. ‡Present addresses: Max-Planck-Institute für Mikrostrukturphysik, Weinberg 2, 06120 Halle, Germany (E.L.); Institut Jean Lamour (UMR CNRS 7198), Université de Lorraine, 54500 Vandoeuvre-lès-Nancy, France (J.C.R.-S.). *e-mail: juan-carlos.rojas-sanchez@univ-lorraine.fr; manuel.bibes@cnrs-thales.fr

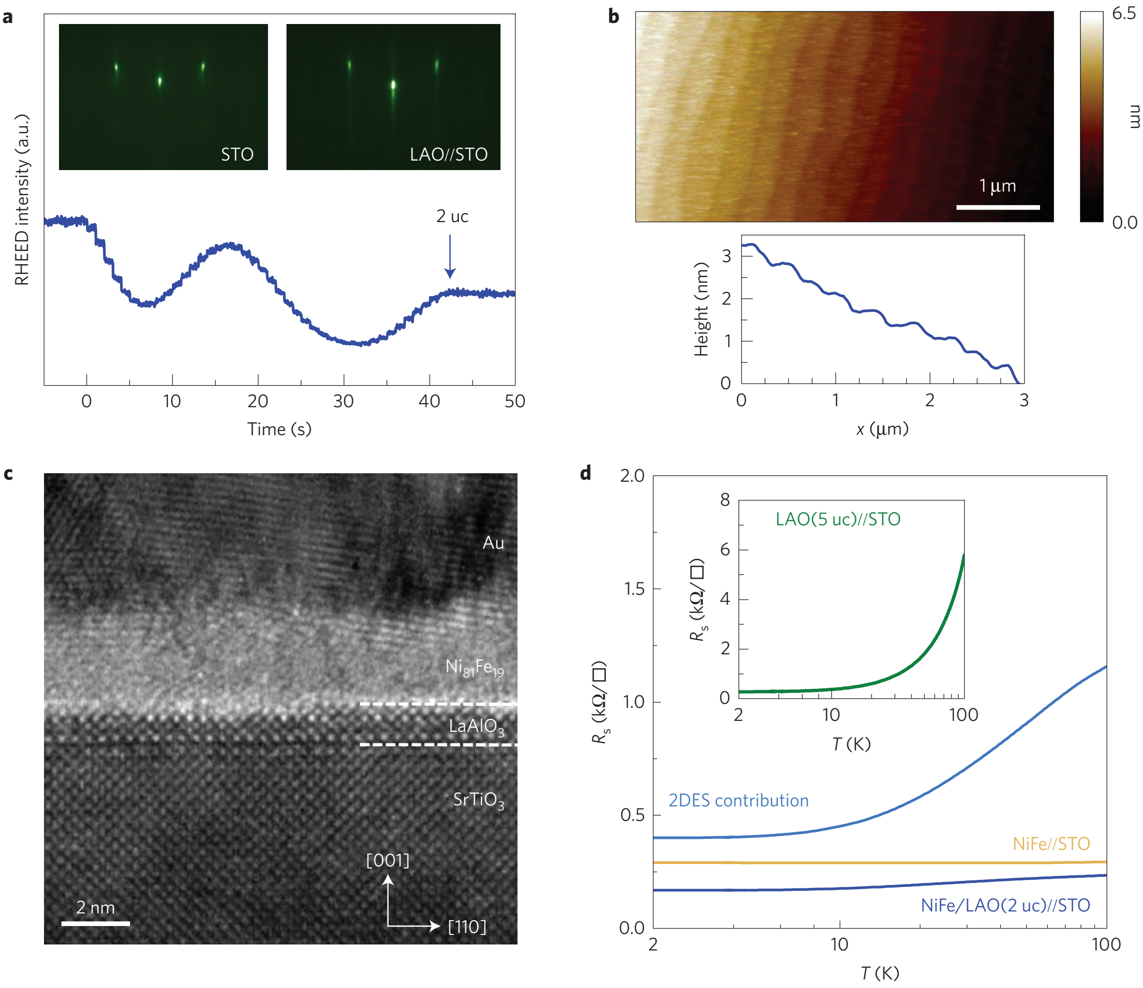

Figure 1 | Characterization of NiFe/LAO//STO system. a, RHEED oscillations during the growth of the 2-uc LAO film and RHEED diffraction patterns before (left inset) and after (right inset) growth. **b**, Atomic force microscopy (AFM) image of the NiFe/LAO(2 uc)//STO sample surface. **c**, Scanning TEM cross-section of the NiFe/LAO(2 uc)//STO sample. **d**, Temperature dependence of the sheet resistance of a NiFe(2.5 nm)/LAO(2 uc)//STO sample and of a reference NiFe(2.5 nm)//STO sample. The extracted resistance of the 2DES is also displayed. Inset: Measured sheet resistance of a standard LAO(5 uc)//STO sample.

(see Methods). The interface between LAO and NiFe is smooth, with limited interaction between the two materials.

In Fig. 1d we compare the temperature dependence of the sheet resistance (R_S versus T) for a typical NiFe(2.5 nm)/LAO(2 uc)//STO sample and a reference NiFe(2.5 nm)//STO single film (see Methods). While the latter shows a weak resistance change between room and low temperatures, the former exhibits a clear resistance decrease. These transport data indicate the presence of an additional conductive channel in the NiFe/LAO(2 uc)//STO sample just as in Co/LAO(1-2 uc)//STO samples[25]. Assuming parallel conduction between the NiFe metal layer and this extra channel, we extract a resistivity versus temperature of the 2DES present in STO that is reminiscent of conventional LAO/STO 2DES behaviour (see the R versus T data of a standard uncapped LAO(5 uc)//STO sample in the inset). From the analysis of Hall and magnetoresistance data in a parallel resistance model, we extract a total carrier density in the 2DES of $n_{\mathrm{total}} \approx 2.6 \times 10^{13}\ \mathrm{cm}^{-2}$ ($n_{\mathrm{total}} = n_1 + n_2$, $n_1 = 1.54 \times 10^{13}\ \mathrm{cm}^{-2}$ and $n_2 = 1.07 \times 10^{13}\ \mathrm{cm}^{-2}$, with mobilities $\mu_1 = 3{,}300\ \mathrm{cm}^2\ \mathrm{V}^{-1}\ \mathrm{s}^{-1}$ and $\mu_2 = 160\ \mathrm{cm}^2\ \mathrm{V}^{-1}\ \mathrm{s}^{-1}$; see Supplementary Note 1 and Supplementary Fig. 1). We conclude that a 2DES is formed in STO in our NiFe/LAO(2 uc)//STO heterostructures, hence enabling the prospect of spin pumping[26] from NiFe into the 2DES.

Next, we characterized the dynamic magnetic response of our samples using ferromagnetic resonance (FMR) at room temperature (see Methods). Figure 2a displays the field derivative of the imaginary part of the dynamic magnetic susceptibility χ'' for different frequencies f of the microwave excitation, as a function of the external magnetic field $H_{\mathrm{d.c.}}$. For a NiFe(20 nm)/LAO(2 uc)//STO sample and a NiFe(20 nm)//LAO reference, we obtain the frequency dependence of the resonance field H_{res} and the peak-to-peak linewidth ΔH_{pp} (see Fig. 2b and c, respectively). The dispersion relation of H_{res} with $\omega = 2\pi f$ (Fig. 2b) follows the trend given by Kittel's relation:

$$\left(\frac{\omega}{\gamma}\right)^2 = (H_{\mathrm{res}})(\mu_0 M_{\mathrm{eff}} + H_{\mathrm{res}}) \tag{1}$$

with μ_0 the vacuum permeability, M_{eff} the effective saturation magnetization and $\gamma = g^* \mu_B/\hbar$, where g^* is the effective electron g-factor (taken to be 2.11 for NiFe, ref. 27), $\hbar$ is the reduced Planck constant and μ_B the Bohr magneton. From Fig. 2c we also determine the effective Gilbert-like damping parameter $\alpha_{\mathrm{NiFe/2DES}}$ according to

$$\Delta H_{\mathrm{pp}}(f) = \Delta H_{\mathrm{inh}} + \frac{2}{\sqrt{3}}\left(\frac{2\pi f}{g^* \mu_B}\right)\hbar \alpha_{\mathrm{NiFe/2DES}} \tag{2}$$

where ΔH_{inh} is the frequency-independent linewidth contribution (arising from inhomogeneities in the ferromagnet (FM)). The

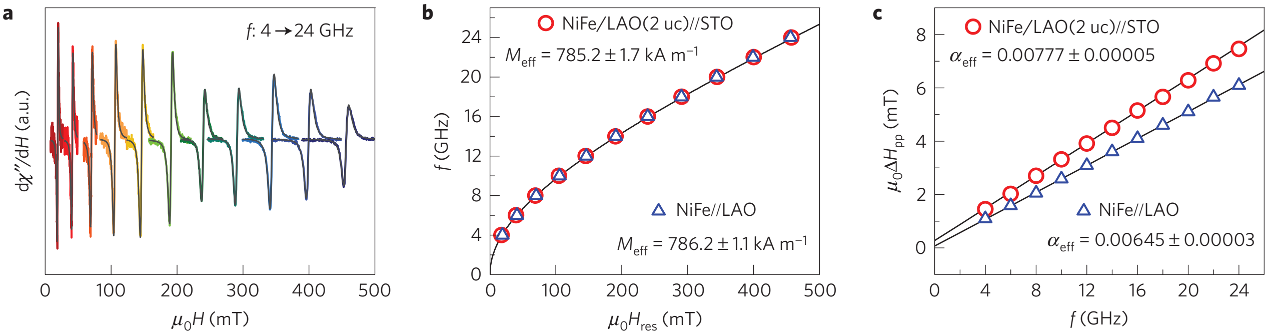

Figure 2 | Ferromagnetic resonance in NiFe/LAO//STO. a, FMR signal at room temperature for microwave frequencies ranging from 4 to 24 GHz in steps of 2 GHz. **b**, Dependence of the FMR resonance frequency on the external magnetic field for a NiFe/LAO//STO sample and a NiFe//LAO reference. **c**, Dependence of the spectral peak-to-peak linewidth with the microwave frequency for the same two samples. Solid black lines in **b** and **c** are fits to the data using equations (1) and (2), respectively.

effective damping for the NiFe(20 nm)/LAO(2 uc)//STO sample is enhanced compared to the reference ($\alpha_{\rm NiFe/2DES} = 7.77 \times 10^{-3}$ versus $\alpha_{\rm NiFe} = 6.45 \times 10^{-3}$), which is consistent with spin absorption/dissipation in the 2DES[26].

To inject a spin current into the LAO/STO interface states and detect the IEE, we use a spin-pumping technique in which the out-of-equilibrium distribution generated in a ferromagnet by FMR enables the ejection of a pure spin current from the ferromagnet (towards an adjacent conducting material), as theoretically described by Tserkovnyak *et al.*[26], with details on the experiments and analysis reviewed by Azevedo *et al.*[28] and Harder and colleagues[29]. At $T = 7$ K, spins are pumped from NiFe into the LAO/STO 2DES and we measure the voltage generated into the 2DES (spin-to-charge conversion) in the geometry sketched in Fig. 3a (see Methods). In spin-pumping experiments, a prerequisite to the production of a sizeable charge current is the transmission of the out-of-equilibrium spin accumulation generated on the FM metal side to the non-magnetic (NM) layer. Whereas in all-metal systems the spin accumulation easily diffuses from the FM to the NM, this diffusion is impeded if a thin insulating layer is inserted at the FM/NM interface[30]. If the NM is a 2DES, as here, the strongly localized character of the wavefunctions may however allow an exchange coupling between the FM and the NM, and enable a substantial non-equilibrium spin accumulation to appear in the 2DES. Alternatively, spin accumulation may also be produced in the 2DES through spin conduction by hopping processes via localized states with long spin lifetime in the LAO[31] (see Supplementary Note 2).

Figure 3b displays the FMR response for positive and negative $H_{\rm d.c.}$ at 7 K and a back-gate voltage of +125 V and Fig. 3c shows the detected raw voltage (normalized by the microwave power) and its decomposition into symmetric ($V_{\rm sym}$) and antisymmetric ($V_{\rm asym}$) components, for positive and negative $H_{\rm d.c.}$. The symmetric component largely dominates the signal, and is almost perfectly reversed upon reversing $H_{\rm d.c.}$, as expected from spin-to-charge conversion effects with which $V_{\rm sym} \propto j_s \times \sigma$ (with j_S being the spin current and σ the spin direction, which changes sign upon switching the direction of $H_{\rm d.c.}$). As in ISHE experiments, magnetotransport effects such as anisotropic magnetoresistance or the planar Hall effect are probably responsible for the antisymmetric signal, and yet can also contribute to the symmetric part[28,29]. For comparison we show similar data for a reference NiFe(20 nm)//LAO sample (inset of Fig. 3c): the detected voltage is almost perfectly antisymmetric, evidencing the absence of spin-to-charge conversion in this sample and ruling out any contribution from the NiFe//LAO interface to the data measured in NiFe/LAO//STO. We thus conclude that spin-pumping and spin-to-charge conversion effects in the 2DES are responsible for the signal reported in the main panel of Fig. 3c. The interfacial charge current density corresponding to this value of the symmetric component of the measured voltage is simply given by $j_C^{\rm 2D} = V_{\rm sym}/(wRh_{\rm rf}^2) = 53.3$ mA m^{-1} G^{-2} with $R = 35.25\ \Omega$ being the resistance of the NiFe/LAO//STO heterostructure and $w = 0.4$ mm being the sample width. Remarkably this value of $j_C^{\rm 2D}$ is much larger than in previous reports (1.5 mA m^{-1} G^{-2} for Ag/Bi, ref. 24, and 5.9 mA m^{-1} G^{-2} for α-Sn, ref. 32).

The most likely mechanism giving rise to spin-to-charge conversion into a 2DES with a sizeable Rashba effect such as the LAO/STO system is the so-called inverse Edelstein effect (IEE). In this picture, the spin current pumped in the interfacial Rashba 2DES selectively relaxes into the two spin–orbit split Fermi surfaces (see Fig. 3d). In the IEE framework, this leads to a shift of the Fermi contours in momentum space (see Fig. 3e), thereby producing a lateral interfacial charge current density[24,33]. A quantitative analysis of the IEE requires estimating the pumped spin current density from the relation:

$$j_S = \frac{g^{\uparrow\downarrow}\gamma^2\hbar(\mu_0 h_{\rm rf})^2}{8\pi\alpha^2_{\rm NiFe/2DES}}\left[\frac{\mu_0 M_{\it eff}\gamma + \sqrt{(\mu_0 M_{\it eff}\gamma)^2 + 4\omega^2}}{(\mu_0 M_{\it eff}\gamma)^2 + 4\omega^2}\right]\left(\frac{2e}{\hbar}\right) \quad (3)$$

with γ the gyromagnetic ratio in NiFe, $h_{\rm rf}$ the microwave field amplitude. $g^{\uparrow\downarrow}$ is the real part of the spin-mixing conductance given by

$$g^{\uparrow\downarrow} = \frac{4\pi M_{\it eff}\, t_{\rm F}}{g^* \mu_{\rm B}}\left(\alpha_{\rm NiFe/2DES} - \alpha_{\rm NiFe}\right) \quad (4)$$

with $t_{\rm F} = 20$ nm the thickness of the NiFe film.

From the out-of-plane angular dependence of the FMR signal at 7 K, we can extract $\alpha_{\rm NiFe/2DES}$ at this temperature (see Supplementary Note 3 and Supplementary Fig. 2), which yields $\alpha_{\rm NiFe/2DES} = 7.7 \times 10^{-3}$, comparable to the room-temperature value. From equations (3) and (4) we obtain $g^{\uparrow\downarrow} = 13.3$ nm^{-2}, in the range of reported values for interfacial systems[24,34], and $j_s = 8.4 \times 10^6$ A m^{-2} G^{-2}. Combining this value with the measured 2D charge current yields the spin-to-charge current conversion efficiency parameterized by the inverse Edelstein length $\lambda_{\rm IEE} = j_C^{\rm 2D}/j_S$.

$\lambda_{\rm IEE}$ is the figure of merit characterizing the efficiency of the conversion of a three-dimensional (3D) spin current into a 2D charge current. Physically, in the simplified approximation of one single Fermi contour, $\lambda_{\rm IEE}$ corresponds to the distance the electrons would travel in the 2DEG between collisions occurring with a characteristic time τ while having their spin direction locked with respect to their momentum due to the Rashba SOI. For the data shown in Fig. 3b, we find $\lambda_{\rm IEE} = 6.4$ nm. This value of $\lambda_{\rm IEE}$ in our NiFe/LAO/STO samples is one order of magnitude larger than the values of 0.1–0.4 nm found at Bi/Ag interfaces[24] and other Rashba interfaces[35], and is also larger than $\lambda_{\rm IEE} = 2.1$ nm found at the

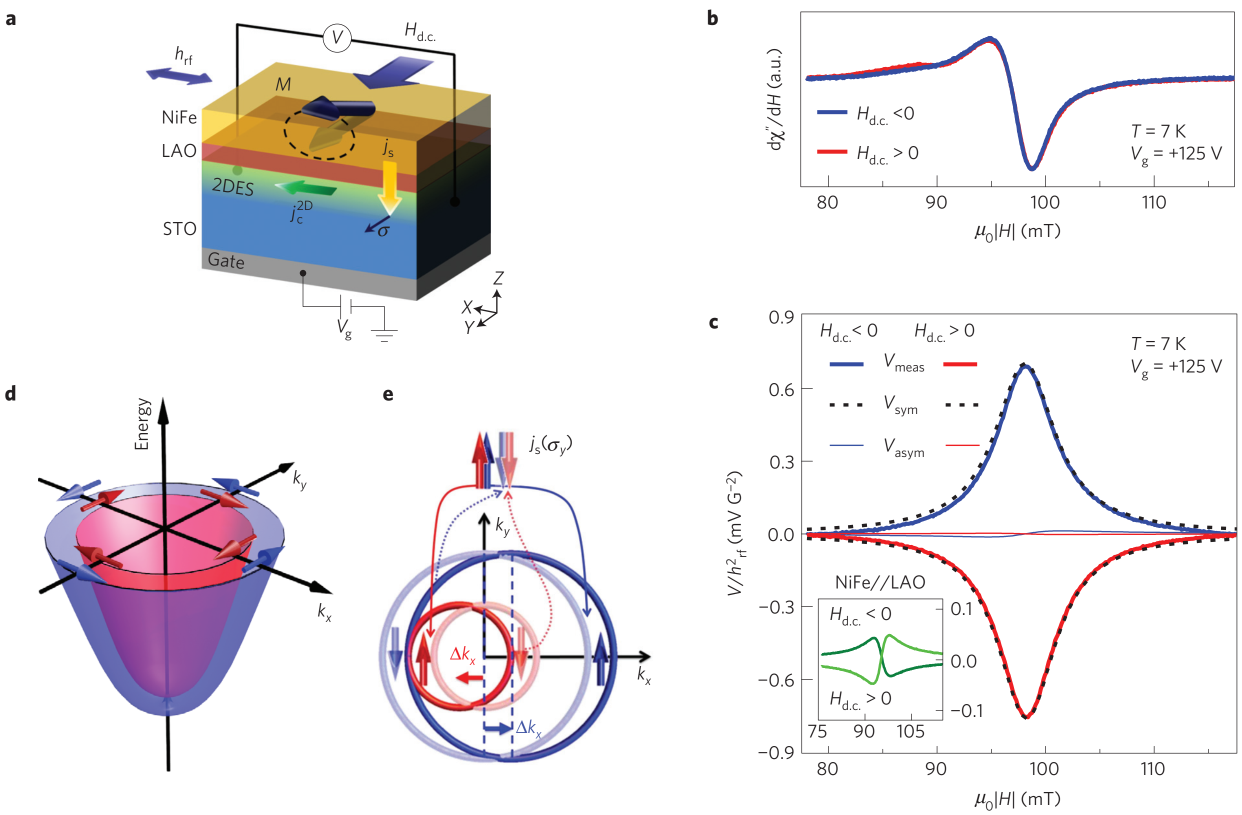

Figure 3 | Spin-to-charge conversion in LAO//STO 2DES. a, Sketch of spin-pumping experimental configuration. Measurements were performed in a cylindrical X-band resonator cavity ($f \approx 9.6$ GHz) at 7 K. **b**, FMR signal at negative and positive external magnetic fields, at a gate voltage of +125 V. **c**, Detected voltage normalized to the square of the amplitude of the rf field (thick solid lines) at negative and positive external magnetic fields at $V_g = +125$ V. The decomposition into symmetric (dotted lines) and antisymmetric (thin solid lines) components is also plotted. Inset: detected voltage for a NiFe//LAO reference. **d**, Sketch of a simplified Rashba-type system at equilibrium. At the Fermi level there are two Fermi contours (one sketched in blue, the other in red) with opposite spin textures (the blue and red arrows show the spin direction of the electrons on the outer and inner contour, respectively). **e**, Principle of the inverse Edelstein effect: the injection of a current j_S of spins oriented along y (σ_y) from the ferromagnet creates an accumulation of spin-up ($\sigma_y > 0$) electrons (darker blue and red arrows) and a depletion of spin-down ($\sigma_y < 0$) electrons (lighter blue and red arrows). This accumulation/depletion process shifts the two inequivalent Fermi contours, which generates a transverse charge current along x.

surface of the topological insulator α-Sn (ref. 32). This spin-to-charge conversion efficiency also compares favourably with what is measured in heavy metals. In such systems, the interconverted spin and charge currents are both 3D and the figure of merit is the spin Hall angle θ_{SHE}, which amounts to 0.056 in Pt, 0.12 in Ta and 0.37 in W (ref. 10). For comparison purposes, one can convert the value of θ_{SHE} into λ_{IEE} through $\lambda_{IEE} = \theta_{SHE} l_{sf}$ (l_{sf} is the spin diffusion length), which yields 0.2 nm for Pt, 0.3 nm for Ta and 0.43 nm for W, well below the $\lambda_{IEE} = 6.4$ nm in our LAO/STO system.

At a Rashba interface, in the simplified approximation of circular spin contours, λ_{IEE} can be expressed as a function of the momentum relaxation time τ and the Rashba coefficient α_R (refs 24,33)

$$\alpha_R = \frac{\hbar \lambda_{IEE}}{\tau} \tag{5}$$

Interpreting $\lambda_{IEE} = 6.4$ nm (for $V_g = 125$ V) from equation (5) with a value of the Rashba coefficient $\alpha_R \sim 3 \times 10^{-12}$ eV m, in the range expected from calculations[37] or derived from weak antilocalization measurements[15,38] leads to $\tau \sim 1.4$ ps, two orders of magnitude above the similar IEE relaxation time at Rashba or topological insulator interfaces with metals. This is consistent with the existence of additional relaxation mechanisms induced in 2DEGs by the proximity with metals and the expected protection of a slow relaxation by an insulating layer (LAO in our system), as discussed in ref. 32. We can also note that $\tau \sim 1.4$ ps is consistent with the mobility $\mu = 4{,}000$–$5{,}000$ cm^2 V^{-1} s^{-1} (at this gate voltage, the ungated mobility, $\mu = 3{,}300$ cm^2 V^{-1} s^{-1}, is expected to increase by 20–50%; see ref. 36) and an effective electron mass $m^* \approx 2m_0$ ($m_0 = 9.1 \times 10^{-31}$ kg).

The large dielectric constant of the STO substrate and the relatively low carrier density of the LAO/STO 2DES makes it possible to use a back-gate voltage V_g to modulate the 2DES carrier density (by 0.5–1 × 10^{11} cm^{-2} V^{-1}, refs 36,39) and electronic properties. As we show in Fig. 4a,b, back-gating has a dramatic influence on the spin-to-charge conversion efficiency. The detected charge current evolves from a moderate positive value at negative V_g (charge depletion regime), to a small positive value at $V_g = 0$, and then becomes negative for positive gate voltage, showing a maximum amplitude around +125 V. This is summarized by the gate dependence of λ_{IEE} displayed in Fig. 4c, from which a crossover between positive to negative spin-to-charge conversion is clearly visible near $V_g = 0$.

The gate dependence of the IEE signal in our samples is highly non-trivial and probably related to the multiband nature of the 2DES electronic structure, and the possibility to tune the 2DES across Lifshitz points with the gate[39]. As pointed out in several studies[39,40], at low carrier density the electrons occupy a single low-lying band with d_{xy} character, whereas raising the Fermi level E_F through the application of a gate voltage promotes the population of $d_{xz,yz}$ bands. The amplitude of α_R and the associated spin textures are strongly dependent on the relative energy and the orbital symmetry of these bands[37,39,41], which provides some grounds on which we build a tentative interpretation of our results. First-principles

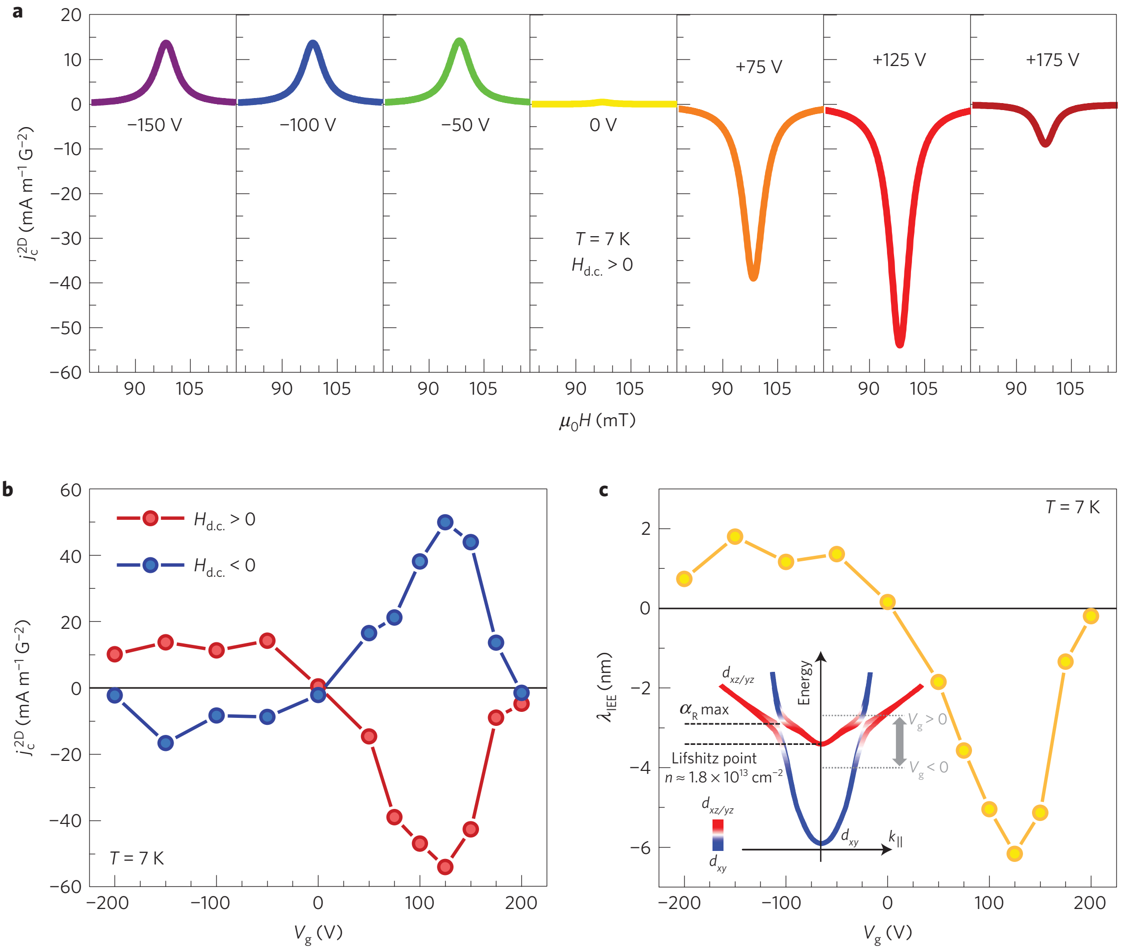

Figure 4 | Gate control of the inverse Edelstein effect in LAO//STO 2DES. a, Symmetric component of the detected signal for different gate voltages. **b**, Gate dependence of the signal amplitude at positive and negative external magnetic fields. **c**, Gate dependence of the figure of merit of the inverse Edelstein effect λ_{IEE}. Inset : sketch of the band structure of the 2DES, adapted from refs 37,39,42.

calculations indicate that, for the low-lying d_{xy} band, α_R is weak and has a negative sign, whereas, for the $d_{xz,yz}$ bands, α_R is positive and increases from the band bottom to the avoided crossing point with d_{xy} (refs 37,39,42). Accordingly, the influence of spin–orbit effects on charge and spin transport strongly depends on the position of the Fermi level—that is, on the gate voltage. With a carrier density of $\sim 2.6 \times 10^{13}$ cm^{-2} at $V_g = 0$, the Fermi levels in our sample sits just above the bottom of the lowest $d_{xz,yz}$ band (corresponding to $1.7–1.9 \times 10^{13}$ cm^{-2}, refs 36,39), and both d_{xy} and $d_{xz,yz}$ bands are populated. Assuming that α_R has an opposite sign for the two populated bands[37], spin-to-charge conversion effects tend to compensate each other, consistent with the low value of j_C^{2D} we measure at $V_g = 0$.

At negative gate voltages, E_F decreases, and only the d_{xy} band with weak α_R is populated, which is in line with our observation of an increase in j_C^{2D} when increasing V_g from 0 towards negative voltages, levelling off at a moderate value, consistent with the weak energy dependence of the Rashba splitting expected for this band. At positive gate voltages, E_F increases, and eventually reaches the avoided crossing between d_{xy} and $d_{xz,yz}$, where α_R is the largest[39,40,42] and has a sign opposite to that of the d_{xy} band. This maximum of the Rashba splitting was reported to occur at carrier densities $n \approx 3.3 \times 10^{13}$ cm^{-2} (ref. 40), which is accessible with back-gate voltages on the order of +100 V, consistent with the position of the maximum at +125 V in Fig. 4c. Beyond that point, the Rashba splitting decreases[39,40]. Although, ideally, spin- and angle-resolved photoemission experiments would have to be performed to ascertain the band structure of the 2DES in our NiFe/LAO//STO samples, the above scenario accounts for our observation of an increased j_C^{2D} (in absolute value) at positive gate voltage, and its maximum.

In summary, we have measured a very large spin-to-charge conversion efficiency in the 2DES present at the interface between LaAlO$_3$ and SrTiO$_3$. Conversion occurs through the inverse Edelstein effect arising from the Rashba coupling present at the interface. Upon application of a gate voltage, the amplitude of the converted current can be modulated over one order of magnitude, and even changes sign. This can be interpreted in terms of a crossover between the occupancy of one to several bands with different orbital characters and different spin–orbit textures. Our results suggest that oxide interfaces have a strong potential for spintronics[43], both for the generation or detection of spin currents through direct[22] or inverse Edelstein[24,33] effects, and for their electrical modulation, *à la* Datta & Das[44]. More generally, our observation of a very large spin-to-charge conversion efficiency at an interface with a moderate Rashba splitting highlights the importance of a long scattering time, and calls for the design of novel Rashba interfaces in which confinement and electrical insulation from metallic layers are carefully engineered.

Methods

Methods and any associated references are available in the online version of the paper.

Received 18 February 2016; accepted 8 July 2016;
published online 29 August 2016

References

1. Imada, M., Fujimori, A. & Tokura, Y. Metal–insulator transitions. *Rev. Mod. Phys.* **70,** 1039–1263 (1998).
2. Bibes, M. & Barthélémy, A. Oxide spintronics. *IEEE Trans. Electron Devices* **54,** 1003–1023 (2007).
3. Bowen, M. *et al*. Nearly total spin polarization in $La_{2/3}Sr_{1/3}MnO_3$ from tunneling experiments. *Appl. Phys. Lett.* **82,** 233–235 (2003).
4. Chu, Y. *et al*. Electric-field control of local ferromagnetism using a magnetoelectric multiferroic. *Nat. Mater.* **7,** 478–482 (2008).
5. Liu, L. *et al*. Spin-torque switching with the giant spin Hall effect of tantalum. *Science* **336,** 555–558 (2012).
6. Demidov, V. E., Urazhdin, S., Edwards, E. R. J. & Demokritov, S. O. Wide-range control of ferromagnetic resonance by spin Hall effect. *Appl. Phys. Lett.* **99,** 2013–2016 (2011).
7. Brüne, C. *et al*. Evidence for the ballistic intrinsic spin Hall effect in HgTe nanostructures. *Nat. Phys.* **6,** 448–454 (2010).
8. Hoffmann, A. Spin Hall effects in metals. *IEEE Trans. Magn.* **49,** 5172–5193 (2013).
9. Niimi, Y. & Otani, Y. Reciprocal spin Hall effects in conductors with strong spin–orbit coupling: a review. *Rep. Prog. Phys.* **78,** 124501 (2015).
10. Sinova, J., Valenzuela, S. O., Wunderlich, J., Back, C. H. & Jungwirth, T. Spin Hall effects. *Rev. Mod. Phys.* **87,** 1213–1260 (2015).
11. Witczak-Krempa, W., Chen, G., Kim, Y. B. & Balents, L. Correlated quantum phenomena in the strong spin–orbit regime. *Annu. Rev. Condens. Matter Phys.* **5,** 57–82 (2014).
12. Hwang, H. Y. *et al*. Emergent phenomena at oxide interfaces. *Nat. Mater.* **11,** 103–113 (2012).
13. Ohtomo, A. & Hwang, H. Y. A high-mobility electron gas at the $LaAlO_3/SrTiO_3$ heterointerface. *Nature* **427,** 423–426 (2004).
14. Thiel, S., Hammerl, G., Schmehl, A., Schneider, C. W. & Mannhart, J. Tunable quasi-two-dimensional electron gases in oxide heterostructures. *Science* **313,** 1942–1945 (2006).
15. Caviglia, A. D. *et al*. Tunable Rashba spin–orbit interaction at oxide interfaces. *Phys. Rev. Lett.* **104,** 126803 (2010).
16. Ben Shalom, M., Sachs, M., Rakhmilevitch, D., Palevski, A. & Dagan, Y. Tuning spin–orbit coupling and superconductivity at the $SrTiO_3/LaAlO_3$ interface: a magnetotransport study. *Phys. Rev. Lett.* **104,** 126802 (2010).
17. Caprara, S., Peronaci, F. & Grilli, M. Intrinsic instability of electronic interfaces with strong Rashba coupling. *Phys. Rev. Lett.* **109,** 196401 (2012).
18. Bucheli, D., Grilli, M., Peronaci, F., Seibold, G. & Caprara, S. Phase diagrams of voltage-gated oxide interfaces with strong Rashba coupling. *Phys. Rev. B* **89,** 195448 (2014).
19. Seibold, G., Caprara, S., Grilli, M. & Raimondi, R. Intrinsic spin Hall effect in systems with striped spin–orbit coupling. *Europhys. Lett.* **112,** 17004 (2015).
20. Bychkov, Y. A. & Rashba, E. I. Properties of a 2D electron gas with lifted spectral degeneracy. *JETP Lett.* **39,** 78–81 (1984).
21. Manchon, A., Koo, H. C., Nitta, J., Frolov, S. M. & Duine, R. A. New perspectives for Rashba spin–orbit coupling. *Nat. Mater.* **14,** 871–882 (2015).
22. Edelstein, V. M. Spin polarization of conduction electrons induced by electric current in two-dimensional asymmetric electron systems. *Solid State Commun.* **73,** 233–235 (1990).
23. Aronov, A. G. & Lyanda-Geller, Y. B. Nuclear electric resonance and orientation of carrier spins by an electric field. *JETP Lett.* **50,** 431–433 (1989).
24. Rojas-Sánchez, J. C. *et al*. Spin-to-charge conversion using Rashba coupling at the interface between non-magnetic materials. *Nat. Commun.* **4,** 2944 (2013).
25. Lesne, E. *et al*. Suppression of the critical thickness threshold for conductivity at the $LaAlO_3/SrTiO_3$ interface. *Nat. Commun.* **5,** 4291 (2014).
26. Tserkovnyak, Y., Brataas, A. & Bauer, G. E. W. Enhanced Gilbert damping in thin ferromagnetic films. *Phys. Rev. Lett.* **88,** 117601 (2002).
27. Shaw, J. M., Nembach, H. T., Silva, T. J. & Boone, C. T. Precise determination of the spectroscopic g-factor by use of broadband ferromagnetic resonance spectroscopy. *J. Appl. Phys.* **114,** 243906 (2013).
28. Azevedo, A., Vilela-Leão, L., Rodríguez-Suárez, R., Lacerda Santos, A. & Rezende, S. Spin pumping and anisotropic magnetoresistance voltages in magnetic bilayers: theory and experiment. *Phys. Rev. B* **83,** 144402 (2011).
29. Harder, M., Cao, Z. X., Gui, Y. S., Fan, X. L. & Hu, C.-M. Analysis of the line shape of electrically detected ferromagnetic resonance. *Phys. Rev. B* **84,** 054423 (2011).
30. Mosendz, O., Pearson, J. E., Fradin, F. Y., Bader, S. D. & Hoffmann, A. Suppression of spin-pumping by a MgO tunnel-barrier. *Appl. Phys. Lett.* **96,** 2010–2013 (2010).
31. Reyren, N. *et al*. Gate-controlled spin injection at $LaAlO_3/SrTiO_3$ interfaces. *Phys. Rev. Lett.* **108,** 186802 (2012).
32. Rojas-Sánchez, J.-C. *et al*. Spin to charge conversion at room temperature by spin pumping into a new type of topological insulator: α-Sn films. *Phys. Rev. Lett.* **116,** 096602 (2016).
33. Shen, K., Vignale, G. & Raimondi, R. Microscopic theory of the inverse Edelstein effect. *Phys. Rev. Lett.* **112,** 096601 (2014).
34. Jamali, M. *et al*. Giant spin pumping and inverse spin Hall effect in the presence of surface and bulk spin–orbit coupling of topological insulator Bi_2Se_3. *Nano Lett.* **15,** 7126–7132 (2015).
35. Nomura, A., Tashiro, T., Nakayama, H. & Ando, K. Temperature dependence of inverse Rashba–Edelstein effect at metallic interface. *Appl. Phys. Lett.* **106,** 212403 (2015).
36. Fête, A. *Magnetotransport Experiments at the $LaAlO_3/SrTiO_3$ Interface* (Université de Genève, 2014).
37. Shanavas, K. V., Popović, Z. S. & Satpathy, S. Theoretical model for Rashba spin–orbit interaction in d electrons. *Phys. Rev. B* **90,** 165108 (2014).
38. Hurand, S. *et al*. Field-effect control of superconductivity and Rashba spin–orbit coupling in top-gated $LaAlO_3/SrTiO_3$ devices. *Sci. Rep.* **5,** 12751 (2015).
39. Joshua, A., Pecker, S., Ruhman, J., Altman, E. & Ilani, S. A universal critical density underlying the physics of electrons at the $LaAlO_3/SrTiO_3$ interface. *Nat. Commun.* **3,** 1129 (2012).
40. Liang, H. *et al*. Nonmonotonically tunable Rashba spin–orbit coupling by multiple-band filling control in $SrTiO_3$-based interfacial electron gases. *Phys. Rev. B* **92,** 075309 (2015).
41. King, P. D. C. *et al*. Quasiparticle dynamics and spin–orbital texture of the $SrTiO_3$ two-dimensional electron gas. *Nat. Commun.* **5,** 3414 (2014).
42. Zhong, Z., Tóth, A. & Held, K. Theory of spin–orbit coupling at $LaAlO_3/SrTiO_3$ interfaces and $SrTiO_3$. *Phys. Rev. B* **87,** 161102 (2013).
43. Bibes, M. *et al*. Towards electrical spin injection into $LaAlO_3/SrTiO_3$. *Phil. Trans. R. Soc. A* **370,** 4958–4971 (2012).
44. Datta, S. & Das, B. Electronic analog of the electro-optic modulator. *Appl. Phys. Lett.* **56,** 665–667 (1990).

Acknowledgements

Research at CNRS/Thales received support from the ERC Consolidator Grant #615759 "MINT" and the region Île-de-France DIM "Oxymore" (project NEIMO). Support from the ANR SOspin and ANR Lacunes projects is also acknowledged. H.N. was partly supported by the Leading Young Researcher Overseas Visit Program, JSPS Grant-in-Aid for Scientific Research (B) (#15H03548). Authors are grateful to Y. Kodama (Tohoku University, Japan) for TEM observation and to N. Reyren for his help at the early stage of the project.

Author contributions

M.B., L.V., E.L., J.C.R.-S., H.J. and J.-M.G. conceived and designed the experiment. M.B. and L.V. supervised the project. E.L. and D.C.V. grew the samples with the help of H.N. and E.J., and performed the d.c. transport experiments and analysed the data. E.L., J.C.R.-S., Y.F., S.O. and J.-M.G. performed the room-temperature FMR measurements and analysed the data. Y.F., S.O., J.C.R.-S., E.L. and L.V. performed the low-temperature spin-pumping experiments and analysed the data with the help of M.B., H.J. and A.F. M.B. and E.L. wrote the manuscript, with inputs from H.J. All authors discussed the data and contributed to the manuscript.

Additional information

Supplementary information is available in the online version of the paper. Reprints and permissions information is available online at www.nature.com/reprints. Correspondence and requests for materials should be addressed to J.C.R.-S. or M.B.

Competing financial interests

The authors declare no competing financial interests.

Methods

Sample growth. We follow the sample fabrication procedure described in ref. 25. The $LaAlO_3$ (LAO) films were grown by pulsed laser deposition on 5 mm × 5 mm TiO_2-terminated (001)-oriented $SrTiO_3$ (STO) substrates (from Crystec GmbH). A single-crystal LAO target was ablated by a KrF (248 nm) excimer laser at a repetition rate of 1 Hz and with a fluence of $\sim$1 J cm^{-2}. The LAO deposition was performed in an oxygen partial pressure of 2.0×10^{-4} mbar and at a substrate temperature of 730 °C. The substrate-to-target distance was 63 mm. After LAO growth, the samples were then annealed for 30 min at an oxygen pressure of approximately 400 mbar at 500 °C. Finally, the LAO//STO heterostructures were cooled at 25 °C min^{-1} and kept in the same oxygen pressure for $\sim$30–60 min. PLD growth was followed by *in situ* deposition of a metallic $Ni_{81}Fe_{19}$ layer by d.c. magnetron sputtering at room temperature in a pure Ar atmosphere, capped by Au or Al. For the NiFe//LAO reference sample, the NiFe layer was deposited on a (001)-oriented LAO substrate and capped with Al.

Transmission electron microscopy. A specimen for TEM observation was prepared using a combination of mechanical polishing and ion milling. The energy for Ar ion milling was gradually decreased from 4 to 1 keV to minimize ion-beam-induced damage. The same strategy was applied for focused ion beam energy from 30 to 4 keV. TEM analysis was performed using JEOL TEMs operated at 300 keV.

d.c. transport. The samples were electrically contacted with aluminium wires by ultrasonic wedge bonding. The contacts penetrate in depth through the whole AlO_x/NiFe/$LaAlO_3$//$SrTiO_3$ stack (whose total thickness is only a few nanometres), therefore electrically connecting the two conducting layers NiFe and $SrTiO_3$ in parallel. The longitudinal and transverse d.c. transport properties of the samples were measured in a Quantum Design Dynacool system as a function of temperature and magnetic field (up to ±9 T). We estimated the sheet resistance contribution (versus T) of the 2DES to the measured sheet resistance of the NiFe/LAO(2 uc)//STO sample in the framework of a parallel conduction model, following ref. 25. The carrier density and mobility in the 2DEG were deduced from the fitting to the measured Hall and longitudinal magnetoresistance data of a NiFe/LAO//STO sample and a NiFe//STO reference, following ref. 45 and using one and two carrier types for the metal and the 2DES, respectively (see Supplementary Note 1 for details).

FMR and voltage measurements with applied back gate. Frequency-dependent ferromagnetic resonance (Fig. 2) was performed at room temperature by using a broadband technique involving a co-planar waveguide. During each measurement, the microwave frequency was fixed while the external magnetic field was swept. The intensity of each spectrum in Fig. 2a is proportional to the field derivative of the imaginary part of the dynamic magnetic susceptibility ($d\chi''/dH$) obtained by using a lock-in technique and field modulation. By fitting the frequency dependences of the resonance field and linewidth, the effective magnetization M_{eff} and the effective damping constant were obtained, which rules out linewidth broadening due to frequency-independent inhomogeneities. For low-temperature spin-pumping experiments, FMR and d.c. transverse voltage measurements were performed simultaneously on 2.4 mm × 0.4 mm slabs. To realize the electrical connections (sketched in Fig. 3a), a sample holder made of a printed circuit board (PCB) circuit was used. The two contacts at the metallic top layer were connected to the PCB sample holder via Al wire bonding (just as for d.c. transport), and the back gate was connected by gluing the substrate on one contact of the PCB sample holder using conductive silver paint. To perform the measurements, the sample was placed at the centre of a cylindrical X-band cavity ($f \approx 9.6$ GHz, TE_{011} mode). The system was cooled down from room temperature to 7 K using a helium-flow cryostat. At 7 K, the sample was initialized by sweeping the back-gate voltage from +200 V to −200 V, then back to +200 V, at which the first measurement was performed. The spin-pumping measurements were performed at fixed V_g, and between acquisitions V_g was changed monotonously from +200 to −200 V. The linear dependence of the measured d.c. voltage amplitude on the applied power of the microwave excitation has been verified up to around 3 mW at 7 K. For the measurements described in the main text, the microwave power was fixed at 1.99 mW. The quality factor Q of the cavity was measured to calculate the amplitude h_{rf} of the radiofrequency magnetic field. In turn, h_{rf} was used to calculate the injected spin current density j_s due to spin pumping. We checked the reproducibility of the voltage measurements by rotating the sample (rotation axis in-plane) by 180° with respect to the d.c. magnetic field $H_{d.c.}$, which is equivalent to reversing the $H_{d.c.}$ direction (Fig. 3a). The normalized voltage V/h_{rf}^2 is usually slightly different in the parallel ($H_{d.c.}$ applied as shown in Fig. 3a) and antiparallel cases, which is due to the sensitive placement of the sample in the electrical field node of the cavity. In such cases, the interfacial charge current density j_C^{2D} was calculated by averaging the voltages obtained in both directions. The measurements were repeated three times at intervals of several months, showing similar and reproducible results.

References

45. Xu, W. J. *et al*. Anomalous Hall effect in Fe/Gd bilayers. *Europhys. Lett.* **90,** 27004 (2010).